Strain and rotation rate from GPS in Tibet, Anatolia, and the Altiplano

Richard W. Allmendinger,[1] Robert Reilinger,[2] and Jack Loveless[1]

[1] Deformation measured by regional GPS networks in continental plateaus reflects the geologic and tectonic variability of the plateaus. For two collisional plateaus (Tibet and Anatolia) and one noncollisional (the Altiplano), we analyze the regional strain and rotation rate by inverting GPS velocities to calculate the full two-dimensional velocity gradient tensor. To test the method, we use gridded velocities determined from an elastic block model for the eastern Mediterranean/ Middle East region and show that to a first order, the deformation calculated directly from the GPS vectors provides an accurate description of regional deformation patterns. Principal shortening and extension rate axes, vertical axis rotation, and two-dimensional (2-D) volume strain (dilatation) are very consistent with long-term geological features over large areas, indicating that the GPS velocity fields reflect processes responsible for the recent geologic evolution of the plateaus. Differences between geological and GPS descriptions of deformation can be attributed either to GPS networks that are too sparse to capture local interseismic deformation, or to permanent deformation that accrues during strong earthquakes. The Altiplano has higher internal shortening magnitudes than the other two plateaus and negative 2-D dilatation everywhere. Vertical axis rotation changes sign across the topographic symmetry axis and is due to distributed deformation throughout the plateau. In contrast, the collisional plateaus have large regions of quasi-rigid body rotation bounded by strike-slip faults with the opposite rotation sense from the rotating blocks. Tibet and Anatolia are the mirror images of each other; both have regions of positive dilatation on the outboard sides of the rotating blocks. Positive dilatation in the Aegean correlates with a region of crustal thinning, whereas that in eastern Tibet and Yunnan province in China is associated with an area of vertical uplift. Rollback of the Hellenic trench clearly facilitates the rotation of Anatolia; rollback of the Sumatra–Burma trench probably also enables rotation about the eastern syntaxis of Tibet. **Citation:** Allmendinger, R. W., R. Reilinger, and J. Loveless (2007), Strain and rotation rate from GPS in Tibet, Anatolia, and the Altiplano, *Tectonics*, *26*, TC3013, doi:10.1029/ 2006TC002030.

1. Introduction

[2] Continental plateaus have captivated the attention of geoscientists since before the advent of plate tectonics. Of the two largest plateaus, Tibet is the result of the collision of the Indian continent with Asia, whereas the Altiplano has formed in a noncollisional environment with simple subduction of the oceanic Nazca plate beneath South America. The widespread availability of GPS data in the last 15 years provides a significant new perspective on the instantaneous state of strain in continental plateaus that have evolved over tens of millions of years. To use GPS data to understand plateau evolution, we must investigate the relationship between instantaneous, elastic, interseismic deformation and the longer-term, permanent geologic deformation.

[3] We calculate regional strain and rotation rates from GPS velocity fields for Anatolia, Tibet, and the Altiplano (Figure 1) and compare them to existing first-order geologic structures. Previous analyses of strain in these areas commonly use velocity gradients calculated along one-dimensional transects [e.g., *Banerjee and Bürgmann*, 2002; *Zhang et al.*, 2004; *Reilinger et al.*, 2006], reflecting the fact that early GPS networks were commonly one-dimensional (1-D) transects. Recently, however, sufficient data have become available in these areas to calculate the full two-dimensional velocity gradient tensor, providing a much richer picture of horizontal surface deformation [*England and Molnar*, 2005; *Flesch et al.*, 2005; *Kahle et al.*, 2000], albeit one with some ambiguities.

2. Methods

[4] Because of their great utility for understanding the earthquake cycle, the most common analysis of GPS data involves elastic modeling of the locking depth of the known faults [e.g., *Banerjee and Bürgmann*, 2002; *Bevis et al.*, 2001; *Brooks et al.*, 2003; *Khazaradze and Klotz*, 2003; *Norabuena et al.*, 1998; *Reilinger et al.*, 2000]. One can then subtract from the observed GPS velocity field the velocity vectors calculated from the best fitting elastic model [see *Meade and Hager*, 2005; *Reilinger et al.*, 2006]. These residual velocities, commonly very small

---

[1]Department of Earth and Atmospheric Sciences, Cornell University, Ithaca, New York, USA.
[2]Department of Earth, Atmospheric, and Planetary Sciences, Massachusetts Institute of Technology, Cambridge, Massachusetts, USA.
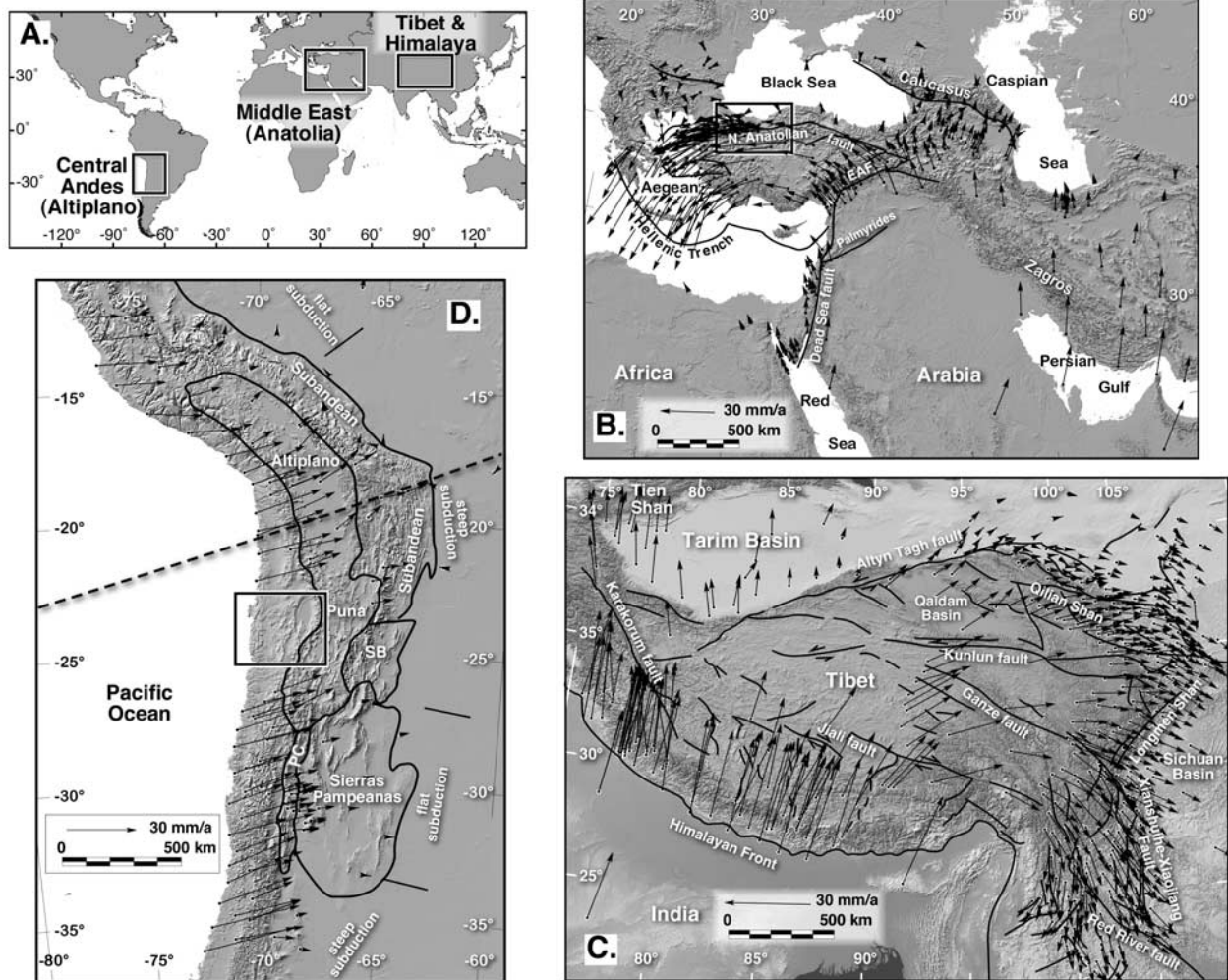
Figure 1. (a) Map showing location of the three plateaus described in this paper. (b–d) Detailed maps of the three areas on a GTOPO30 shaded relief map base. Black arrows in are GPS velocity vectors; individual maps and arrows are not at the same scale. See original publications for data and errors. Selected structures and/or structural provinces shown for reference. (b) Map of the eastern Mediterranean/Middle East; EAF, East Anatolian fault. GPS data are from *Reilinger et al.* [2006]. Small black box shows the location of Figure 10. (c) Map of Tibet and surrounding region. GPS data are from *Zhang et al.* [2004]. (d) Map of the central Andes with GPS data from *Kendrick et al.* [2001] and *Brooks et al.* [2003]. Straight-line segments in the foreland show the approximate boundaries of regions underlain by flat and steep subduction. Black dashed line is topographic symmetry plane from *Gephart* [1994]. PC, Precordillera; SB, Santa Barbara System. Box shows location of Figure 12.

and very nearly random in orientation, are thought by some to represent the permanent component of the deformation [e.g., *Khazaradze and Klotz*, 2003].

2.1. Velocity Gradients in Two Dimensions

[5] Modern GPS networks are, at a regional scale at least, much more spatially complete than earlier networks, thus allowing us to calculate the two-dimensional velocity gradient tensor. This tensor is defined as

$$u_i = t_i + \frac{\partial u_i}{\partial x_j} x_j = t_i + e_{ij} x_j, \qquad (1)$$

where u_i is the GPS measured velocity of the station, t_i is a constant of integration that corresponds to the displacement at the origin of the coordinate system, x_j is the position of the station, and e_{ij} is the displacement rate (velocity)

gradient tensor. Because there are six unknowns in two dimensions (e_{11}, e_{12}, e_{21}, e_{23}, t_1, and t_2), data from at least three noncolinear stations are needed. We rewrite the equations as [*Williams and Kane*, 1999; *Shen et al.*, 1996]

$$
\begin{bmatrix}
{}^1u_1 \\
{}^1u_2 \\
{}^2u_1 \\
{}^2u_2 \\
\cdots \\
\cdots \\
{}^nu_1 \\
{}^nu_2
\end{bmatrix}
=
\begin{bmatrix}
1 & 0 & {}^1x_1 & {}^1x_2 & 0 & 0 \\
0 & 1 & 0 & 0 & {}^1x_1 & {}^1x_2 \\
1 & 0 & {}^2x_1 & {}^2x_2 & 0 & 0 \\
0 & 1 & 0 & 0 & {}^2x_1 & {}^2x_2 \\
\cdots & \cdots & \cdots & \cdots & \cdots & \cdots \\
\cdots & \cdots & \cdots & \cdots & \cdots & \cdots \\
1 & 0 & {}^nx_1 & {}^nx_2 & 0 & 0 \\
0 & 1 & 0 & 0 & {}^nx_1 & {}^nx_2
\end{bmatrix}
\begin{bmatrix}
t_1 \\
t_2 \\
e_{11} \\
e_{12} \\
e_{21} \\
e_{22}
\end{bmatrix},
\tag{2}
$$

where n (≥ 3) is the total number of stations. Solving these equations is a classic inverse problem; we use a standard least squares solution to the overconstrained problem [*Menke*, 1984; *Press et al.*, 1986]. For infinitesimal strains, tensor e can be additively decomposed into a strain and rotation rate:

$$
e_{ij} = \varepsilon_{ij} + \omega_{ij} = \left(\frac{e_{ij} + e_{ji}}{2}\right) + \left(\frac{e_{ij} - e_{ji}}{2}\right),
\tag{3}
$$

where ε_{ij} is the infinitesimal strain rate tensor and ω_{ij} is the rotation rate (vorticity) tensor.

2.2. Rotation and Shear Strain Rates

[6] The antisymmetric part of the velocity gradient tensor, ω_{ij}, can be easily recast in terms of an axial vector whose magnitude is equivalent to the magnitude of vertical axis rotation rate, or vorticity [*Malvern*, 1969]. The rotations cited here are with respect to a downward positive vertical axis with clockwise (CW) positive and counterclockwise (CCW) negative, as in normal geological conventions. A convenient measure of overall magnitude of strain rate in a region is the maximum engineering shear strain rate, which is equal to twice the maximum tensor shear strain rate. These two quantities can be thought of as the diameter and radius, respectively, of the Mohr's circle for infinitesimal strain rate; that is the difference of the two principal infinitesimal strain rates. The orientation of the maximum tensor shear strain rate is always at 45° to the principal axes.

2.3. Volume Strain Rates

[7] In three dimensions, the volume strain (dilatation) rate is the first invariant of the infinitesimal strain rate because it does not depend on the coordinate system. The first invariant is equal to:

$$
I_\varepsilon = \varepsilon_{11} + \varepsilon_{22} + \varepsilon_{33} = e_{11} + e_{22} + e_{33}.
\tag{4}
$$

However, the campaign GPS that characterizes most networks does not provide reliable vertical velocities. If we assume constant volume, we can calculate ε_{33} from the negative of the sum of ε_{11} and ε_{22}. This raises the important issue of whether the deformation measured by GPS is constant volume or not; elastic deformation is commonly characterized by Poisson's ratios of ~0.25 whereas a constant volume (i.e., incompressible) deformation would have a Poisson's ratio of 0.5 [*Turcotte and Schubert*, 1982]. Where ($\varepsilon_{11} + \varepsilon_{22}$) < 0, there is an excess of horizontal shortening which should be balanced by vertical extension (thickening); where ($\varepsilon_{11} + \varepsilon_{22}$) = 0, it implies a strike-slip regime with neither thinning nor thickening; and where ($\varepsilon_{11} + \varepsilon_{22}$) > 0, there is an excess of horizontal extension which should be balanced by vertical shortening (thinning). There are, of course, other reasons to doubt a constant volume assumption, as we shall see, below.

2.4. Strain Rate Field From a Velocity Field

[8] Several potential strategies exist for calculating a two-dimensional strain and rotation rate fields from a GPS velocity field, including Delaunay triangulation and various gridded solutions. The problem is poorly defined because of the nonuniform distribution of GPS stations throughout the regions of interest. There are no ideal solutions to this dilemma; thus we take a conservative approach of only interpreting robust regional patterns. Local anomalies are as likely to be artifacts of nonuniform sampling as they are to be real tectonic features.

[9] For gridded solutions, we have used both nearest neighbor and distance weighted approaches. In both analyses, a uniform grid is constructed for the area and the velocity gradients calculated at each node in the grid. The difference in the methods essentially relates to how one selects stations for inclusion in the analysis at each node. In the nearest neighbor method, the gradients are calculated from a fixed number of stations (≥ 3) that are closest to each node. The spatial sensitivity is directly related to the density of GPS stations used and varies across the network.

[10] In the distance weighted approach, all stations in the network are used in the calculation but data from each station are weighted by their distance from the grid node, by specifying a constant, α, that specifies how the effect of a station decays with distance from the node [*Shen et al.*, 1996]. Each datum is weighted by a factor, W:

$$
W = \exp\left(\frac{-d^2}{2\alpha^2}\right),
\tag{5}
$$

where d is the distance between the node and a station. Stations within a 1α distance contribute more than 67% to the least squares solution whereas those at greater than 3α contribute less than 1%. In matrix format, W is represented as a diagonalized matrix and included in the classic linear least squares inversion as [*Menke*, 1984]

$$
\mathbf{m} = \left[\mathbf{G}^T\mathbf{W}\mathbf{G}\right]^{-1}\mathbf{G}^T\mathbf{W}\mathbf{d},
\tag{6}
$$

where $\mathbf{G}$ is the large (2n × 6) design matrix on the right-hand side of equation (2), $\mathbf{d}$ is the column vector of velocities on the left side of (2), and $\mathbf{m}$ is the column vector

of unknown velocity gradients and translations on the right-hand side of (2).

[11] With more than three stations, uncertainties arise both from the errors in the individual velocity vectors and from the assumption that strain is homogenous between the stations. We omit any grid node where the absolute value of the magnitude of interest is less than the one-sigma error (blank boxes). The calculation at each grid node is independent of the calculations at all of the other grid nodes. We do not enforce strain compatibility because there is no unambiguous way of doing so with two-dimensional velocity data typical of regional surveys. Use of the distance-weighted algorithm minimizes strain compatibility problems.

[12] Most of the figures in this paper use a 75 km grid spacing and the distance weighted algorithm with $\alpha = 150$ km. We choose a value of α that yields maximum variation in the parameter of interest with minimum number of insignificant nodes (i.e., where the absolute value of the magnitude is less than the 1 sigma uncertainty). These parameters necessarily result in "smearing" of patterns, making it more difficult to relate steep strain gradients to individual structures. The features and patterns described have been identified using the nearest neighbor method as well. We provide additional plots of shortening, extension, and maximum shear strain rate for all three regions in the auxiliary material.[1]

3. Plateaus

[13] A complete review of geologic setting and previous work in the three plateaus (Figure 1) is far beyond the scope of this paper. Tibet was produced by the collision of India and Asia, and Anatolia results from the collision of the Arabian plate with western Asia and eastern Europe across the Bitlis suture. The evolution of Anatolia is associated with the rollback of the Hellenic-Cyprus Trench and back-arc extension in the Aegean Sea [*Le Pichon and Angelier*, 1979; *Royden*, 1993; *Reilinger et al.*, 2006]. Tibet is bounded, and at least partly constrained by, stable continental blocks underlying the Tarim and Sichuan basins, among others. Both, however, are dominated by large, near vertical strike-slip faults. The Altiplano, in contrast, is noncollisional and is bounded by large, low-angle thrust faults on both sides. These differences not only result in very different geology but probably also influence the character and distribution of elastic deformation that may be captured by the GPS velocity field.

3.1. Anatolian Plateau

[14] The eastern Mediterranean/Middle East data set is a subset of that recently published by *Reilinger et al.* [2006]. The region includes the Arabian Shield, Zagros and Caucasus mountains, the Anatolian block, Aegean Sea, and Hellenic Trench (Figure 2). In northwestern Turkey, the data set only includes GPS observations prior to the 1999 $M_w = 7.5$ Izmit earthquake and thus represents a sample from the interseismic part of the earthquake cycle.
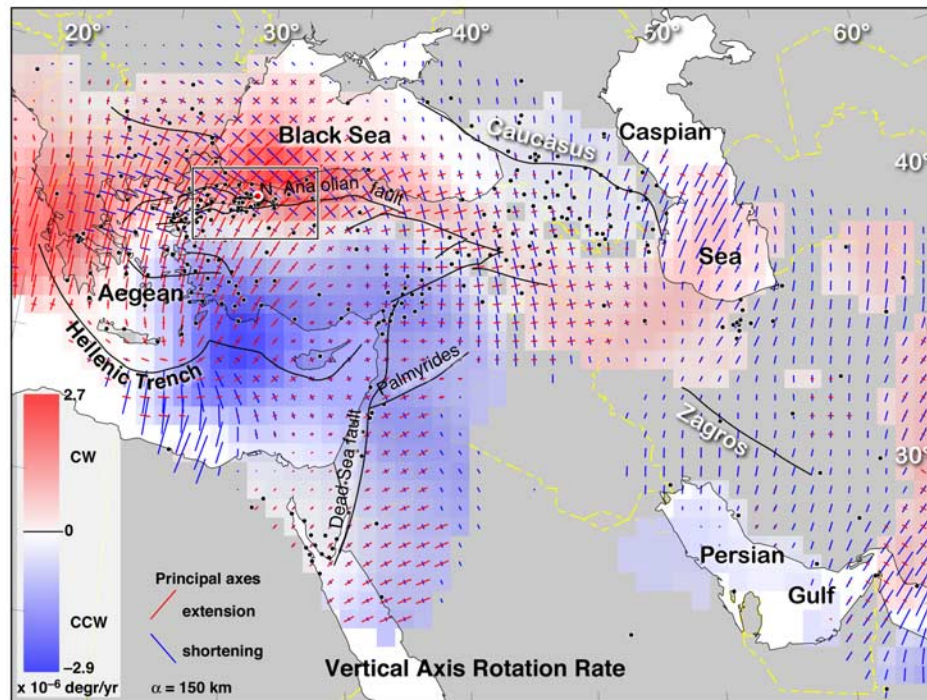
[15] The infinitesimal principal strain rate axes are remarkably consistent with the major, long-term geological structures of the region (Figure 2). The shortening rate axes are almost perfectly oriented at 45° to the fault plane for right-lateral slip on the North Anatolian fault. Likewise, the principal axes are correctly orientated for transtensional deformation along the Dead Sea fault. Shortening axes are normal to the thrust structures in the Caucasus and the Zagros with minor strike parallel extension. The well-known north-south geological extension in the northern Aegean and Gulf of Corinth [*Jackson and McKenzie*, 1984; *Şengör et al.*, 1985] has also been captured by the GPS network. The Arabian Shield, though moving northward at ~20 mm/yr with respect to Eurasia, displays almost no internal strain reflecting both the scarcity of GPS stations and that it probably behaves as a rigid block on GPS timescales.

[16] Two large regions of coherent vertical axis rotation rate are apparent (Figure 2): The counterclockwise rotation of the Anatolian block is occurring at rates of up to $-2.9 \pm 0.09 \times 10^{-6}$°/yr (about -3°/Ma projected to geological timescales) in southwestern Turkey. The Anatolian block is also known for CCW paleomagnetic vertical axis rotations as high as $2-3$°/Ma [*Gürsoy et al.*, 2003], although these areas do not coincide with the largest GPS rotation rates. The region of counterclockwise rotation extends south and eastward to include the region of left-lateral strike-slip on the Dead Sea fault system and the Palmyride transpressional belt. Although the data are too sparse for our method to determine rotation of Arabia, the velocity field clearly shows that broad counterclockwise rotation encompasses all of the Arabian plate and possibly the SW Zagros in Iran.

[17] A belt of clockwise vertical axis rotation rate extends from the northwestern Zagros, along the south side of the Black Sea, the Marmara Sea and into southern Greece (Figure 2), also in agreement with local paleomagnetic data in a narrow zone along the North Anatolian fault [*Tatar et al.*, 1995]. We suspect that this belt is actually quite narrow and is restricted to the region of the North Anatolian fault and its extension into NW Iran, but considerable smearing has occurred because of the paucity of stations farther north and in the Zagros. The largest magnitude vertical axis rotation rates are found at the western end of the North Anatolian fault ($2.7 \pm 0.08 \times 10^{-6}$°/yr), virtually equal in magnitude and opposite in sign from the Anatolian block itself. The high CW rotation rate coincides with a relatively high magnitude of shortening and the western end of a band of high-magnitude extension; all are located near the site of the 1999 Izmit earthquake (red dot in Figure 2). Because these data reflect the preearthquake state of strain, it is tempting to interpret them as precursors to that event. However, the region also has the greatest density of GPS stations anywhere in the area, and thus the anomaly probably just represents normal interseismic strain accumulation that just happened to be more tightly sampled in that area [e.g., *Kahle et al.*, 2000, Figure 7].

[18] While the largest magnitude extension rates occur in the region of the Mamara Sea and Gulf of Corinth, the regions of greatest shortening rate magnitude are located in

---

[1]Auxiliary materials are available in the HTML. doi:10.1029/2006TC002030.

Figure 2. Map of GPS strain and rotation rates for the eastern Mediterranean/Middle East. The principal structures of the region are drawn with heavy black lines and labeled. Principal infinitesimal horizontal strain axes are shown with short colored line segments scaled by the absolute value of their magnitude; red are extension and blue are shortening. Colors in this plot show the variation in magnitude of rotation about a vertical, downward positive axis, with red indicating clockwise (CW) and blue indicating counterclockwise (CCW). Boxes are blank where the absolute value of the magnitude is less than the one sigma error. GPS vectors from *Reilinger et al.* [2006] are shown beneath the semitransparent colors. The red dot shows the epicenter of the 1999 *M*7.5 Izmit earthquake. Box shows the location of the coseismic strain plot shown in Figure 10.

the Caucasus, southeastern Zagros, and between the Hellenic arc and North Africa. Unfortunately, all of these thrust belts are at the edges of the network and thus are not well resolved. Our analyses support the conclusion of *McClusky et al.* [2000] that the SW Aegean has a very low strain rate.

[19] A broad region of negative 2-D dilation (Figure 3) runs from the Caucasus and the Bitlis suture down through the Zagros Mountains. For volume constant deformation, vertical crustal thickening would be needed to balance this excess shortening, which would seem entirely reasonable in these thrust-dominated regions. In the eastern Mediterranean, the dilatation has captured the roll back of the Hellenic trench. Here the shortening between the Hellenic arc and northern Egypt is balanced by back arc extension and crustal thinning (positive 2-D dilatation rate) in the Aegean.

3.2. Tibetan Plateau

[20] *Zhang et al.* [2004] have recently summarized GPS data from more than 500 stations in several networks within and along the margins of the Tibetan Plateau. Regional coverage is very good along the eastern and northeastern

margins of the plateau, and locally in the Himalayas of northern India and Nepal. Data within the plateau are sparse in the east and nonexistent in the west.

[21] As in Anatolia, the principal infinitesimal strain rate axes in Tibet (Figure 4) are consistent with large, long-term geological structures [*England and Molnar, 2005*]. In the Himalayas, large magnitude principal shortening rate axes are oriented orthogonal to the local thrust structures, even though the GPS vectors are not, particularly in northwestern India. Shortening rate axes are smaller, but also nearly orthogonal to thrust structures in the Qilian Shan of northeastern Tibet, even though the velocity vectors are oriented at ∼45° to local strike. Though data are sparse in the Tarim basin [*Zhang et al.*, 2004], the strain rate analysis there, too, coincides with longer-term geologic structure: shortening is virtually nil within the stable Tarim block, but increases and is orthogonal to structures in the southern Tien Shan.

[22] Along the left-lateral Altyn Tagh, Kunlun, Ganze, and Xianshuihe-Xiaojiang fault systems, the instantaneous strain rate axes are close to 45° to the fault zones as expected and even swing around to maintain that angle as the fault zones change strike. Likewise, the infinitesimal
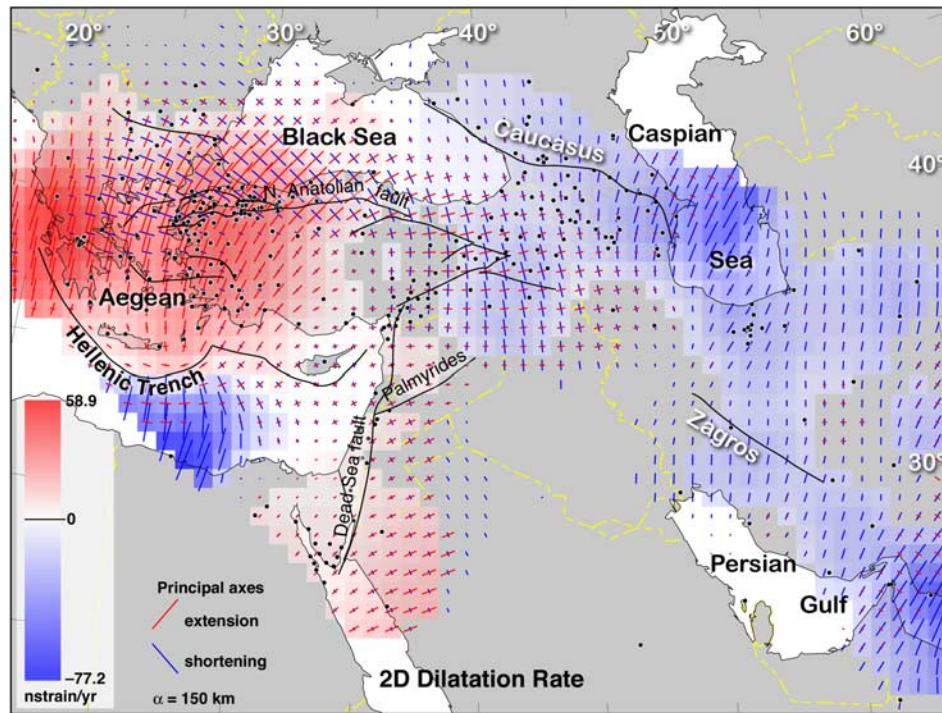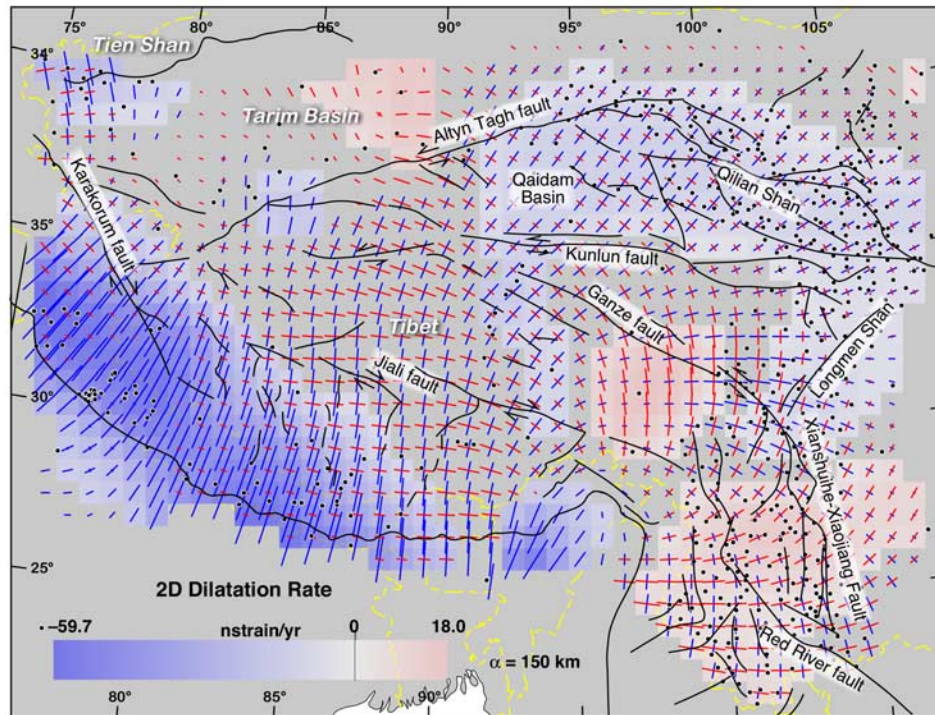
Figure 3. Map showing the magnitude of two-dimensional dilatation rate in the eastern Mediterranean/Middle East.
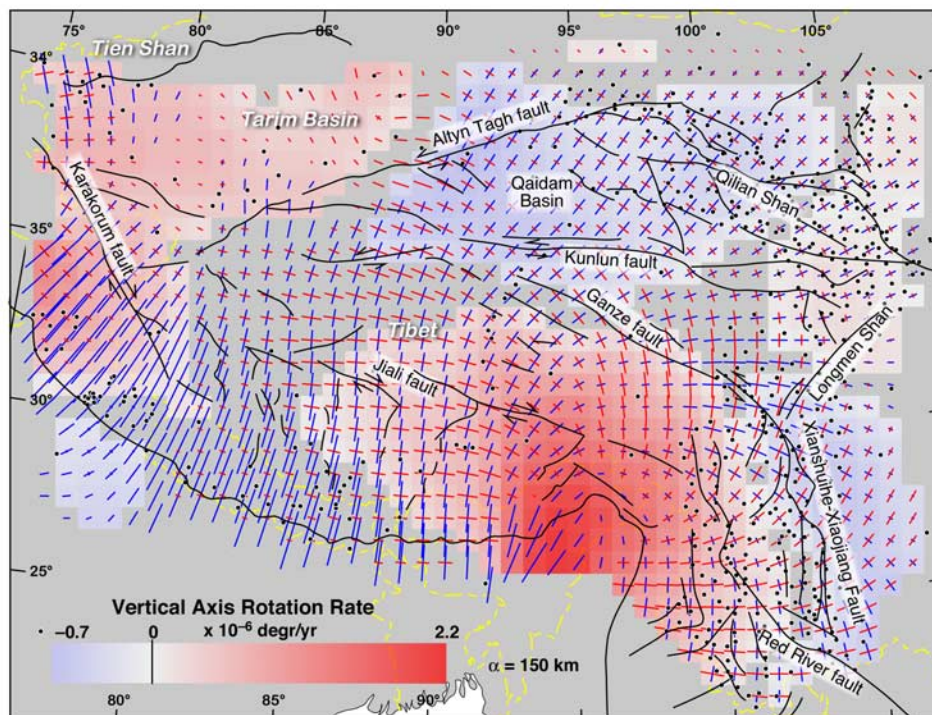
Figure 4. Map of GPS strain and rotation rates for Tibet and the Himalaya. GPS vectors are from *Zhang et al.* [2004]. Major structures are shown with heavy black lines. Other features are as described in Figure 2.

Figure 5. Map of the magnitude of two-dimensional dilatation rate in and around Tibet, calculated from the GPS vectors of *Zhang et al.* [2004]. Red is positive and blue is negative. Other features are as described in Figure 2.

strain rate axes are appropriately orientated for right-lateral strike-slip along the Karakorum fault in the west and the Red River fault in the southeast. Only the Jiali fault of southern Tibet [*Armijo et al.*, 1986] is problematical. Infinitesimal strain rate is consistent with left-lateral slip in the westernmost parts of that structure, but rotates rapidly about the eastern syntaxis so that in the central part of the Jiali fault, the shortening rate axis is perpendicular to the structure and in the eastern part, the extension rate axis is nearly 90° to the fault strike. This would suggest that the Jiali fault may no longer be active as a single coherent right-lateral fault zone.

[23] The principal shortening rate axes around the eastern syntaxis appear to be oriented roughly parallel to the complex India-Eurasia boundary, a pattern that is not easily reconciled with simple continental collision models. The extension perpendicular to the Burma Arc, however, is consistent with back arc extension and roll back of the Burma trench.

[24] The GPS data show several large coherent domains of vertical axis rotation rate (Figure 4). Most obvious is the large region of clockwise rotation around the eastern syntaxis. The maximum magnitude of rotation there, projected over geological timescales, would be equivalent to >2 degrees/ Ma, a conclusion reached independently by *Liu et al.* [2006]. The other major area of clockwise rotation is in the southern Tarim basin and along the Karakorum fault zone. This result is consistent with right-lateral slip on that

major fault and with other geological evidence and reconstructions for the Tarim basin [*Avouac et al.*, 1993].

[25] Two large regions of coherent counterclockwise vertical axis rotation are also present. The region of the Qaidam basin has an average rotation rate of about 6×10^{-7} degrees/yr. These data do not agree well with local geologic evidence [e.g., *Dupont-Nivet et al.*, 2002; *Halim et al.*, 2003] that favors clockwise rotation of the basin; this may be due to smearing of the apparent CCW rotation associated with the two large left-lateral strike-slip faults, the Kunlun and Altyn Tagh. The other region of counterclockwise rotation occurs along the left-lateral Ganze-Xianshuihe-Xiaojiang system of faults along the southeastern margin of Tibet. This region includes the counterclockwise "kink" in the Red River fault recently described by *Schoenbohm et al.* [2006] and suggests that the kink results from broad-scale deformation and that the process is ongoing.

[26] As expected, GPS strain rates are highest along the Himalayas (Figures 4 and 5). The irregular spacing of the network makes it difficult to generalize, but the magnitudes are in the range of -60 ± 10 nstrain/yr. Projected over geological time, this rate would be equivalent to about $60 \pm 10\%$ shortening in 10 million years. Balanced cross sections and other types of horizontal shortening estimates in the region yield about 670 km of shortening in a region that is now 250–300 km wide, a shortening percentage of about 70% since the Eocene [*DeCelles et al.*, 2002]. The extension parallel to the arc of the Himalayas is low (5 ± 2 nstrain/yr),
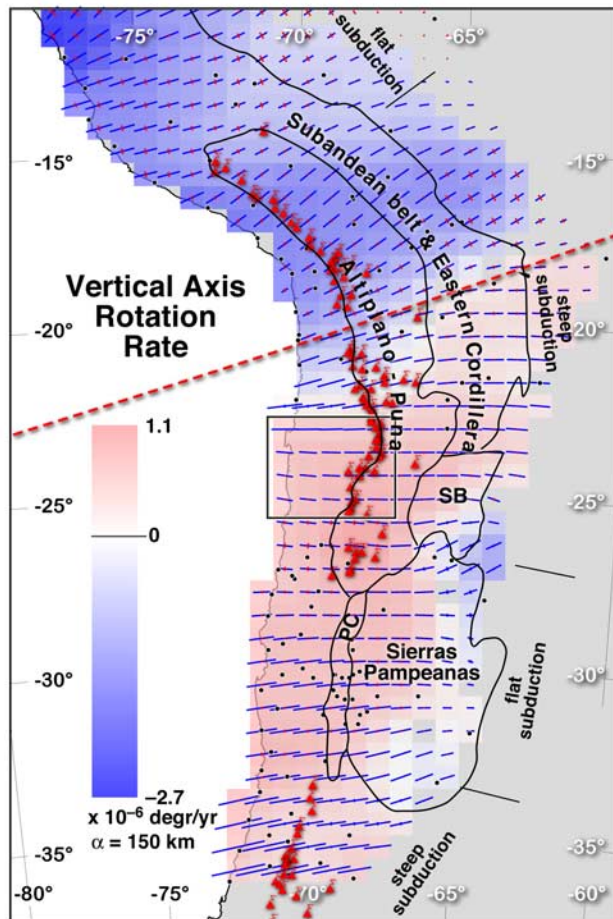
Figure 6. Map of GPS strain and rotation rates for the central Andes, based on data from *Brooks et al.* [2003] and *Kendrick et al.* [2001]. Colors in this plot indicate the magnitude of vertical axis rotation, blue CCW and red CW. Heavy black lines outline the labeled structural provinces; SB, Santa Barbara province; PC, Precordillera fold and thrust belt. Regions underlain by flat and steep (~30° eastward) subduction are indicated at eastern edge of diagram. Red triangles show general distribution of the regions of active arc volcanism, and red dashed line is the Gephart topographic symmetry plane (great circle) [*Gephart,* 1994]. Box shows the location of the detailed study of coseismic strain summarized in Figure 12. Other features are as in Figure 2.

and in one region in NW India corresponding to a structural reentrant, the largest principal horizontal strain rate axis is negative, indicating constriction both N-S and E-W. This strain rate anomaly corresponds to an unusually dense part of the network [*Banerjee and Bürgmann,* 2002] and may well be an artifact of irregular sampling. However, it also coincides with a region of the Himalayan front that has not had a major earthquake since 1400 AD [*Bilham,* 2006; *Bilham et al.,* 2001; *Kumar et al.,* 2006].

[27] Within the plateau, the highest GPS shortening rates occur at the intersection of the Xianshuihe and Longmen Shan faults. This higher shortening rate may simply reflect the greater density of GPS stations there relative to the rest of the plateau. In general, shortening rates within the eastern plateau are reasonably consistent at about -20 ± 10 nstrain/yr, consistent with the simpler 1-D calculations reported by *Zhang et al.* [2004]. Average extension rates are 8.9 ± 2 nstrain/yr. Directly north and east of the syntaxis, shortening rates are markedly lower (-4.8 ± 3.7 nstrain/yr) and extension rates higher (20.5 ± 4.1 nstrain/yr). The northern area is located just to the north of the massive 1950 $M = 8.5$ earthquake [*Bilham et al.,* 2001] and may represent postseismic relaxation (P. Molnar, personal communication, 2006).
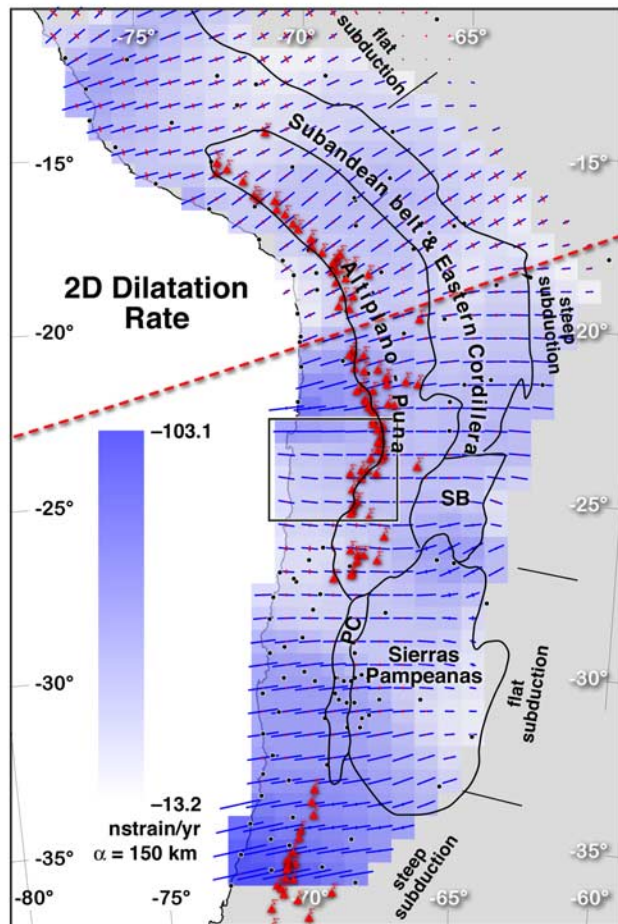
[28] Negative 2-D dilatation (volume strain) rates are associated with the thrust belts in the Himalayas and to a lesser extent the Qilian Shan (Figure 5). In these areas, it is quite reasonable to assume that the excess horizontal shortening is balanced out by vertical extension, that is, crustal thickening. In a mirror image of the Aegean region, a large part of the eastern/southeastern Tibet and Yunnan province has positive 2-D dilatation (excess horizontal extension). However, unlike the Aegean, these regions are not thinning and subsiding but are actively uplifting as shown by the profound entrenchment of major rivers in the area [*Clark et al.,* 2005, 2004; *Schoenbohm et al.,* 2006]. We return to this point in the discussion.

3.3. Altiplano/Puna Plateau

[29] The South American GPS data analyzed here are from *Kendrick et al.* [2001] and *Brooks et al.* [2003]. The former study includes data originally reported by *Norabuena et al.* [1998] but reprocessed using the same reference frame as the other two studies. GPS data from the region between 23° and 26°S have been omitted because that region was perturbed by the 1995 $M = 8.1$ Antofagasta interplate earthquake and the signal there is dominantly coseismic [*Klotz et al.,* 1999]. In general, GPS vectors throughout the Andes (Figure 1) are approximately parallel to the plate convergence direction.

[30] Infinitesimal principal shortening rate axes in the forearc of the central Andes are oriented at a high angle to the plate boundary (Figure 6), even though geologic structures along the coast are dominated by trench-parallel normal faults [*Armijo and Thiele,* 1990; *González et al.,* 2003; *Loveless et al.,* 2005; *Niemeyer et al.,* 1996]. This result stands in marked contrast to the previous two plateaus where the instantaneous deformation is generally consistent with long-term deformation. However, the trench-parallel extensional structures are restricted to a longitudinal zone considerably narrower than the east-west spacing of GPS stations. The true contemporary strain field may indeed be consistent with the long-term deformation demonstrated by these structures, but the sampling interval, both of the GPS data and the gridded strain calculation, is too large to capture this deformation. Infinitesimal shortening rate axes in the back arc, however, are perpendicular to the strike of local thrust faults and folds, just as they are in thrust belts

Figure 7. Map of the magnitude of two-dimensional dilatation rate in the central Andes. Red is positive and blue is negative. Other features are as described in Figure 2.

projected to geological timescales, is identical to the long-term geological shortening rates (−0.33 in 9 ± 1 Ma) in the Subandean belt [*Echavarría et al.*, 2003]. Principal extension rate magnitudes are, almost everywhere in the central Andes, less than 10 nstrain/yr. Along the coast of northern Chile and at the southern end of the region of flat subduction south of the plateau, the greatest principal strain rate axis is negative, indicating horizontal constriction. Both of these areas are dominated by geologic structures that trend at a high angle to the plate boundary [e.g., *Allmendinger et al.*, 2005a].

[32] Unlike Tibet and Anatolia, vertical axis rotations in the Andes are not associated with large strike-slip faults. In contrast, coherent domains of rotation rate (Figure 6) change sign across the topographic symmetry axis [*Gephart*, 1994] that defines the Bolivian orocline [*Allmendinger et al.*, 2005b; *Isacks*, 1988; *Lamb*, 2001b, 2001a]. To the south of this symmetry axis, both instantaneous and long-term vertical axis rotations are clockwise; to the north, both are counterclockwise. If one projects both GPS and paleomagnetic vertical axis rotation to a common time span, they have similar magnitudes though admittedly the errors associated with this projection are large [*Allmendinger et al.*, 2005b].

[33] The two-dimensional volume strain rate in the central Andes (Figure 7) is everywhere negative, indicating an excess of horizontal shortening and, assuming constant volume, crustal thickening. This result is in accord with the general observation that strike-slip and normal faulting are relatively unimportant in the central Andes. Assuming constant volume, the vertical strain rate component, ε_{33} in the Altiplano and Eastern Cordillera would be about 0.4×10^{-7}/yr.

4. Discussion

4.1. Comparison to Elastic Block Models

[34] An alternative approach to analyzing GPS deformation is to assume that all of the interseismic strain occurs at the locked fault boundaries of elastic blocks. In general, the locations of block boundaries are determined from independent geologic and seismic information, while fault slip rates and, when sufficient data are available, fault locking depths are estimated by minimizing the misfit to the GPS velocity field [e.g., *Meade and Hager*, 2005; *Meade*, 2007]. To compare the deformation rate field from the GPS velocities with the elastic block models for the eastern Mediterranean/ Middle East data set [*Reilinger et al.*, 2006], we generated gridded velocities from the block models and calculated the strain and rotation rate from those gridded velocities (Figure 8).

associated with the other plateaus. Infinitesimal extension axes are everywhere small and oriented parallel to the strike of the mountain belt.

[31] Determining regionally consistent magnitudes of infinitesimal strain and rotation rate is difficult in the central Andes because of significantly lower quality GPS data (with fewer repeat observations) in Bolivia and Peru. In general, shortening rate magnitudes in the backarc of the Altiplano and Subandean belt are about −40 ± 4 nstrain/yr, which is about twice as fast as shortening in Tibet, but somewhat less than the shortening rate in the Himalaya. At the southern-most end of the Subandean belt, where GPS data quality is higher, the GPS shortening rate (−37.2 ± 3.5 nstrain/yr),

Figure 8. Comparison of vertical axis rotation calculated from (left) elastic block model velocities to that calculated from (right) the raw GPS velocities. The spacing of the gridded velocities in the block model is 1° by 1°. From top to bottom, the plots show distance-weighted results with $\alpha = 150$ km, $\alpha = 75$ km, $\alpha = 50$ km, and rotations calculated from the eight nearest velocities to each grid node. Only the statistically significant grid nodes are shown. The small black dots in each plot show the locations of velocities used in the solutions. The black lines are the same faults, and total area covered is exactly the same as shown in Figures 2 and 3. The units in each plot are $\times 10^{-6}$ degrees per year.
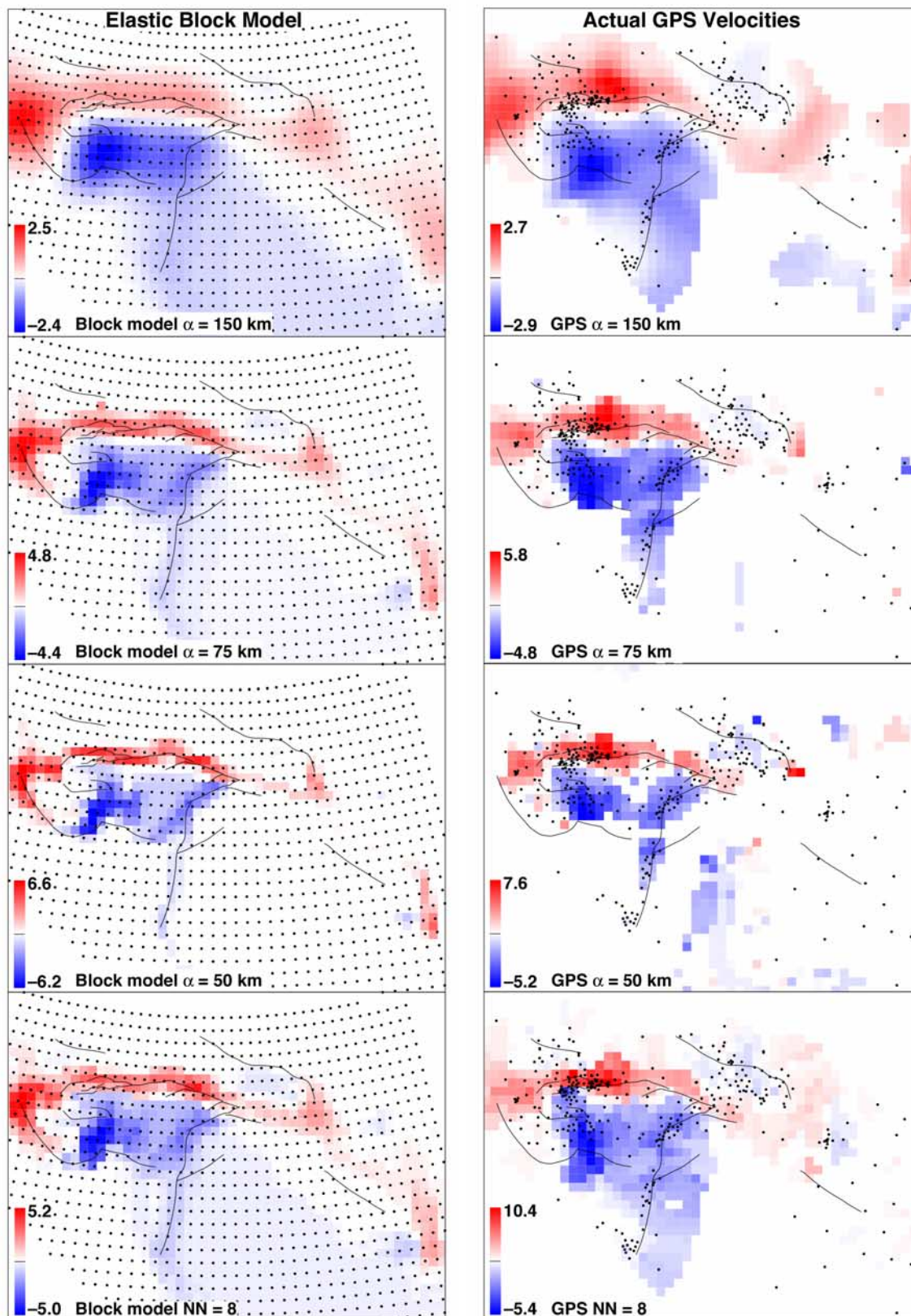
Figure 8

[35] In general, there is excellent agreement, in orientation, magnitude, and spatial distribution, between strain and rotation rates generated from the block model and from the raw GPS velocities (Figure 8). The block model velocities and GPS velocities show the same distribution of CW and CCW rotation rate. Using a distance weighting factor of 150 km in both cases, the belt of CW rotation along the North Anatolian fault is about 400 km wide in the case of the block model and about 300–550 km wide when using the raw GPS velocities. For $\alpha = 75$ km, the belt is 300–350 km wide using the raw velocities and 200–250 km wide with the block model gridded velocities. The range of magnitudes for the block model velocity case, -2.4 to 2.6×10^{-6} degrees/yr, is slightly smaller than for the raw velocities (-2.9 to 2.7×10^{-6} degrees/yr), likely due to the closer spacing of GPS sites than for the gridded block model solution. In these plots, the most obvious artifact produced by the irregular distribution of real stations is the "bulge" in CW vertical axis rotation in the region of the Black Sea, where there are no GPS stations. Though not shown, the same pattern holds for other parameters such as shear strain rate, dilatation rate, etc.

[36] These plots also show the effect of distance weighting on strain rate magnitudes. Halving the aperture (i.e., from 150 to 75 km) nearly doubles the magnitude, in both the block model and the raw GPS velocities. Because we do not know a priori what the appropriate aperture for calculating strain is, magnitudes are important only in a relative sense. That is, the magnitudes of strain and rotation rate in two regions can only be compared when using the same distance weighting function. This problem is inherent to strain, itself, and is not due to irregular network geometries or to rheological assumptions.

[37] Thus, for elastic deformation related to a relatively small number of locked faults, the use of measured GPS velocities, with their highly irregular spacing, results in relatively minor smearing (broadening) of the regions of deformation and amplification of the differences between maximum and minimum values. The experiment does not prove that the deformation is completely elastic because that was an a priori assumption of the block model. Conversely, the broadly distributed strain rate field derived from the block model, which by definition has all strain tightly constrained to block boundaries, demonstrates that available GPS data are not sufficient for our strain rate analysis to depict block-like behavior, a point we return to below.

4.2. Shortening Magnitudes in the Altiplano and Tibet

[38] Both Tibet and the Altiplano have grown during the middle and late Cenozoic. It is somewhat counterintuitive that the smaller of the two, the Altiplano, has a shortening rate about twice as fast. Additionally, except for the northern and southern ends, the Altiplano is essentially aseismic [Chinn and Isacks, 1983] and has no significant horizontal shortening for the last 9 Ma [e.g., Gubbels et al., 1993]. Where minor Quaternary fault scarps are present at the northern and southern limits, they are associated with small normal and strike-slip faults, rather than thrust faults [Cladouhos et al., 1994; Marrett et al., 1994; Sébrier et

al., 1985]. In contrast, Tibet has abundant seismicity and evidence for Quaternary fault activity [Molnar and Chen, 1983; Molnar and Lyon-Caen, 1989; Armijo et al., 1986; Van der Woerd et al., 2002].

[39] The likely explanation for this apparent paradox is that the central Andes are dominated by elastic deformation from the interseismically locked plate boundary. Low-angle dipping boundaries, particularly subduction plate boundaries that are locked to 35–50 km depth [Bevis et al., 2001; Brooks et al., 2003; Norabuena et al., 1998] generate interseismic elastic deformation far broader than vertical intracontinental strike-slip faults that are locked to just 15–20 km depth (Figure 9). Interseismic elastic flexure associated with a locked subduction zone should produce a region of horizontal extension over the locked segment of the fault (Figure 9, left), approximately where forearc normal faults and tension cracks are observed in the central Andes. The Altiplano is also bounded by a low-angle thrust fault on its eastern (retroarc) side. Bevis et al. [2001] have shown that the GPS velocity field can be fit very well by the combined interseismic elastic deformation of both the subduction zone and the Subandean decollement. These models, combined with the lack of geological evidence for post-Miocene shortening and the lack of crustal seismicity in the Altiplano, make a compelling case that the instantaneous deformation in the central Andean plateau is truly elastic. That elastic deformation is converted to permanent deformation by slip on the bounding thrusts, but not by deformation internal to the plateau.

4.3. Two Styles of Rotation

[40] The data sets analyzed here display two distinctly different styles of vertical axis rotation rate. Tibet and Anatolia display large coherent regions of rotation bounded by strike-slip faults with the opposite sense of rotation. They are the mirror images of one another: In Tibet, clockwise rotation about the eastern syntaxis is bounded by counterclockwise rotation along the Ganze-Xianshuihe-Xiaojiang system of left-lateral faults. In the eastern Mediterranean, counterclockwise rotation of Anatolia is bordered by a narrower zone of clockwise rotation on the North Anatolian fault. In both cases, the rotating blocks tend to have low internal strain rates (maximum engineering shear strain rate of 15 nstrain/yr for Anatolia; somewhat less in Tibet) whereas the bounding faults have higher strain rates (50–100 nstrain/yr in Anatolia, ~50 nstrain/yr in Tibet). In other words, the blocks are deforming in a quasi-rigid fashion whereas the bounding faults have high shear strain rates.

[41] Although the central Andes also show coupled clockwise and counterclockwise rotation, none of the rotation is due to rigid body rotation. Vertical axis rotation is always associated with consistent, relatively high values of shear strain rate (maximum engineering shear strain rate values of ~50 ± 5 nstrain/yr) in the absence of discrete bounding strike-slip fault zones. Thus instantaneous bending of the Bolivian orocline occurs by distributed simple shear with lateral gradients in shortening rate diminishing way from the topographic symmetry axis. This is very
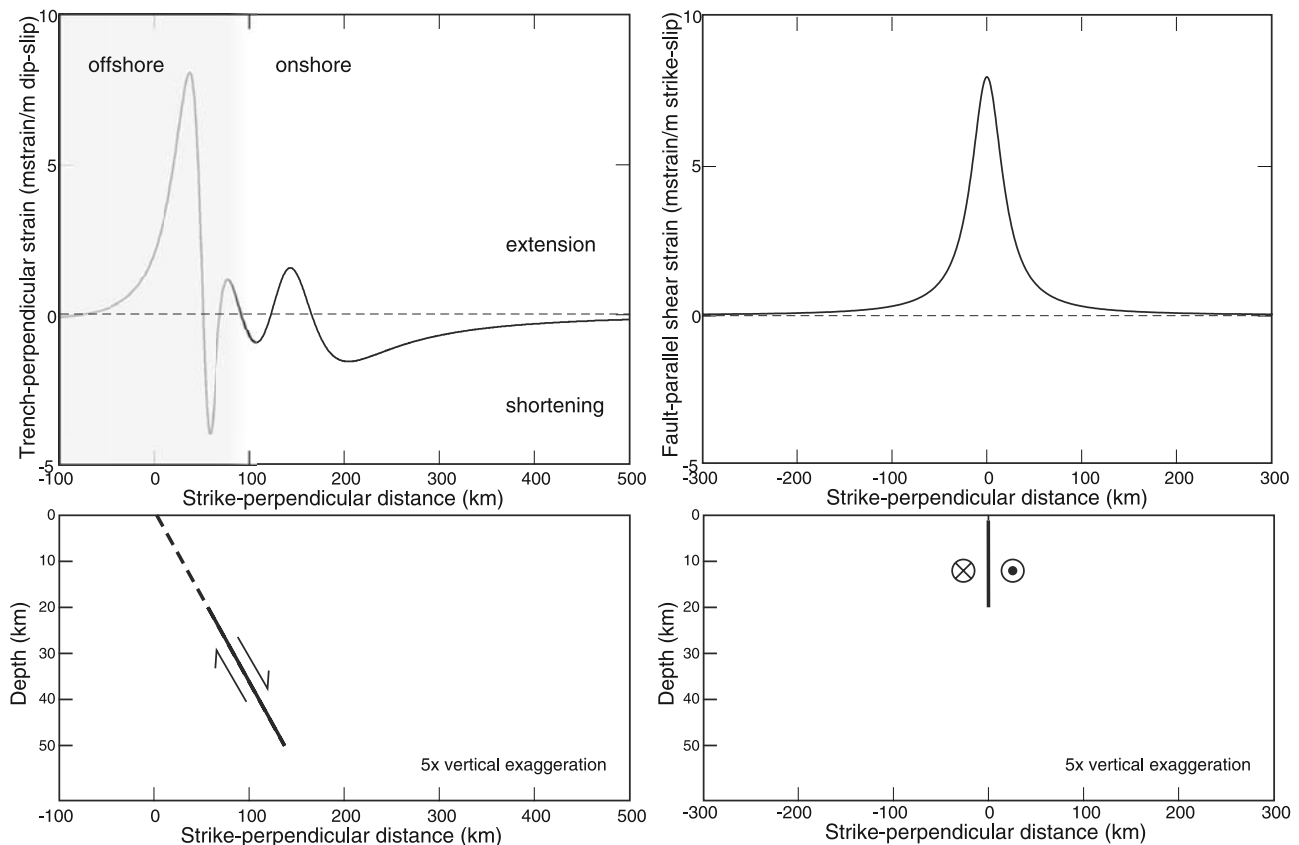
Figure 9. Profiles of surface strain due to unit dislocations in a homogenous elastic half-space. (a) Fault-perpendicular strain due to generic subduction zone model using the back-slip convention of *Savage* [1983], modeled using the algorithms of *Okada* [1985]. Artificial normal fault slip is applied uniformly to the modeled fault (bold black line) between 20 and 50 km depth to simulate interseismic strain accumulation. This depth range is consistent with the extent of the interplate coupling zone inferred from GPS measurements in the central Andes [*Bevis et al.*, 2001]. (b) Magnitude of fault-parallel shear strain due to generic strike-slip model, modeled after *Savage and Burford* [1973] with a locking depth of 20 km, which is broadly consistent with the locking depths determined by the GPS analyses of *Reilinger et al.* [2006] for the North Anatolian fault. The spatial extent of substantial surface strain due to interseismic locking of the subduction fault is far greater than that due to the strike-slip fault.

different than the quasi-rigid block rotation bounded by narrow zones of high simple shear found in the two collisional plateaus.

4.4. Volume Strain Rate

[42] Whereas Tibet and Anatolia display distinct areas of positive and negative 2-D volume strain rate, the central Andes are everywhere negative. The result for the thrust dominated central Andes is consistent with the high rates of GPS shortening. It must also, at least in part be due to nonpermanent (i.e., elastic) deformation around the Altiplano. Shortening deformation during the last 10 Ma has been focused in the Subandean belt on the eastern margin of the plateau (Figures 6 and 7). Many workers have proposed that this shortening produces thickening and uplift at depth beneath the plateau (a "simple shear" thickening [*Allmendinger and Gubbels*, 1996]) and this would

seem to be consistent with the negative 2-D dilatation rate calculated from the GPS data. However, because GPS only measures surface deformation, the 2-D dilatation rate only gives a measurement of the thickening at that point which would be needed to balance the surface measurement in constant volume.

[43] Thrust dominated areas in both Tibet and the eastern Mediterranean/Middle East (Himalayas, Qilian Shan, Caucasus, Zagros) also show negative dilatation. Thickening is entirely expected in these areas, though we cannot tell how the strain captured by GPS is partitioned between permanent deformation and recoverable elastic strain related to the locking of the master decollement in those areas.

[44] Both Anatolia and Tibet show regions of positive 2-D dilatation rate on the "outboard side" of the region of significant rotation. Positive 2-D dilatation, resulting from an excess of horizontal extension and implying crustal thinning, is expected for the Aegean (although the SW
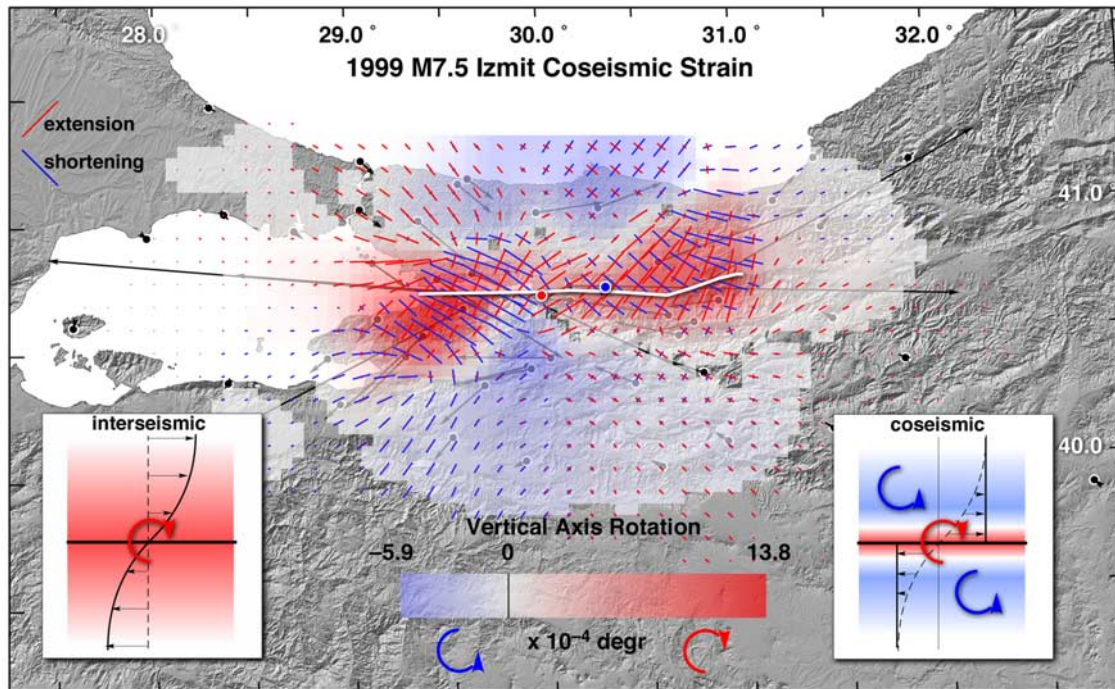
Figure 10. Coseismic vertical axis rotation rate and principal infinitesimal strain rate axes for the 1999 *M*7.5 Izmit earthquake. Analyzed GPS data are from *Reilinger et al.* [2000]. Heavy white line shows the general extent of the ruptured segment of the North Anatolian fault. Insets show the expected deformation patterns for interseismic elastic loading and coseismic elastic rebound.

Aegean has anomalously low GPS extension rate [*Reilinger et al.*, 2006]). Coupled with north-south shortening and negative dilatation rate between the Hellenic Arc and northern Africa, the region presents an excellent example of subduction zone rollback [*Le Pichon and Angelier*, 1979; *Royden*, 1993; *Reilinger et al.*, 2006].

[45] Tibet is a bit less straightforward. By analogy with the Anatolia/Aegean region, the positive 2-D dilatation rate in Tibet should correspond with a region of crustal thinning, perhaps controlled by rollback of the Java-Sumatra trench. However, the geomorphology of eastern Tibet and Yunnan province of China suggests that the region of positive 2-D dilatation rate is one of rapid uplift [*Clark et al.*, 2005, 2004; *Schoenbohm et al.*, 2006], which would be more consistent with thickening. Thus processes beneath the surface, lateral flow and thickening of the middle and/or lower crust or some form of dynamic support from the mantle, may be supporting the high topography of the region [*Beaumont et al.*, 2001, 2004; *Clark and Royden*, 2000; *Nelson et al.*, 1996] rendering the constant volume assumption moot.

[46] Although the geometry of the eastern syntaxis of Tibet is more extreme than the plate corners in the eastern Mediterranean, we suggest that both are influenced by trench roll back. Extension axes in Yunnan Province wrap around to be perpendicular to the Burma arc, with 2-D dilatation rate behind the arc, indicating rollback of the

Burma trench (Figure 5). This conclusion is in agreement with recent mechanical modeling of *Koons et al.* [2006].

4.5. Relations Between GPS and Geological Deformation

[47] In general, all three plateaus display excellent agreement between the orientations of the instantaneous principal strain rate axes and of the geological structures. However, GPS and geological strains are discordant in some areas, most notably in the central Andes. GPS shortening occurs in the Chilean–Peruvian forearc where there is predominantly geological evidence for horizontal extension, possibly an artifact due to GPS station distribution that is too sparse to capture the expected interseismic extension (Figure 9). Likewise, high deformation rates in the Altiplano are probably due to interseismic elastic loading related to the locked subduction plate boundary [*Bevis et al.*, 2001; *Brooks et al.*, 2003; *Khazaradze and Klotz*, 2003; *Norabuena et al.*, 1998]. Interseismic elastic deformation has also been ascribed to the Himalayas and strike-slip faults in the eastern Mediterranean/Middle East [e.g., *Banerjee and Bürgmann*, 2002; *Reilinger et al.*, 2006]. In the eastern Mediterranean/Middle East, the predominance of recoverable elastic strain is supported by the general agreement between GPS-derived and geologic fault slip rates [see *Reilinger et al.*, 2006, Figure 10].
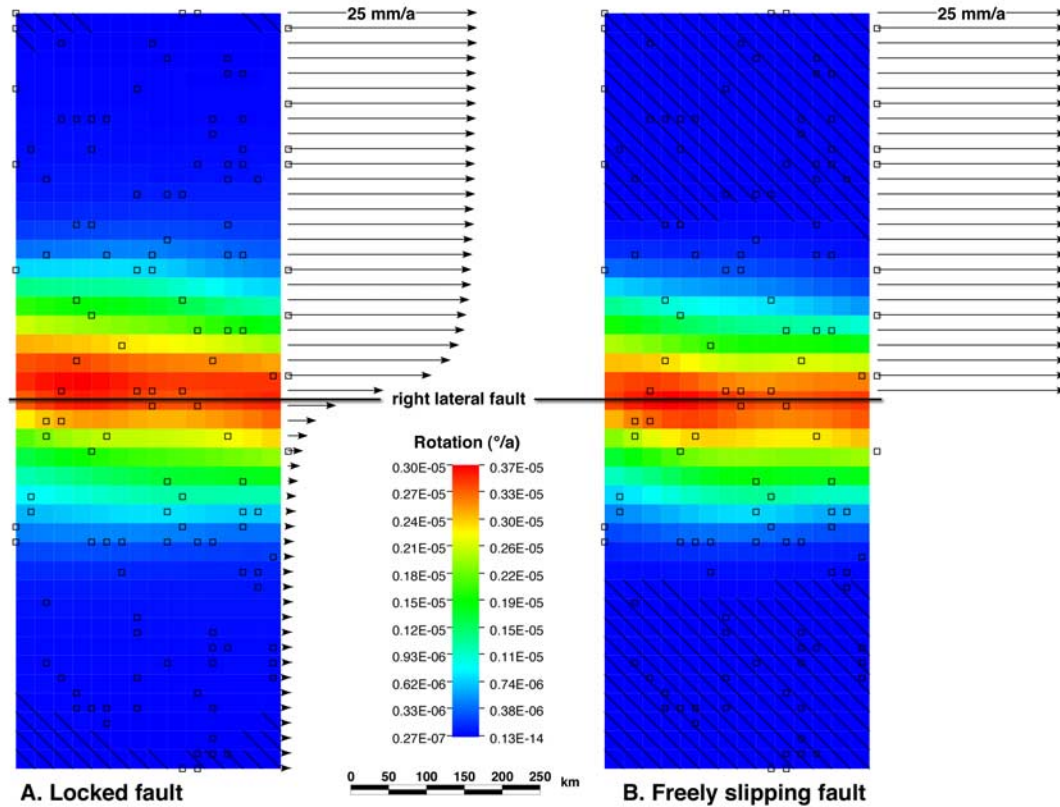
Figure 11. Map views of the vertical axis rotation rate patterns and magnitudes associated with a synthetic, right-lateral strike-slip fault that (a) is locked to 20 km depth and deforms elastically with the displacements shown by the arrows or (b) either a fault that slips freely and permanently or one that has experienced one complete earthquake cycle, as shown by the arrows. In both cases, the far-field displacement rate is 25 mm/yr and the velocity vectors were randomly subsampled to mimic the density of campaign GPS arrays. The vorticity field was smoothed using the distance weighted algorithm with a grid size of 75 km and α = 75 km.

[48] Thus arises an apparent paradox: If the GPS strain and rotation is nonpermanent (i.e., elastic), why should it be so consistent with permanent geological structures over such broad areas (a result also observed in the Basin and Range [*Pancha et al.*, 2006; *Friedrich et al.*, 2003])? We suggest that there are two related answers to this question: First, the elastic strain *should* be the same as the permanent geological strain across faults because it is converted to permanent deformation during earthquakes. It is only in areas relatively close to the fault in question that the coseismic strains are opposite to long-term strains. Second, elastic strain produced by locking of a plate boundary or other major fault can be partially relieved by movement on any fault within the strained region, not just the locked fault, itself. To illustrate these points, we consider two different coseismic strain fields captured by GPS.

4.5.1. The 1999 Izmit, Turkey, Earthquake

[49] The *M*7.5 Izmit earthquake of 1999 provided an excellent record of coseismic displacements to compare with the immediately preceding interseismic deformation already sampled by GPS. Elastic dislocation models of the

event, constructed by fitting geodetic GPS, radar interferometry, surface displacements and earthquake data provide a detailed picture of the fault behavior during this event and the related Dücze event a few months later [e.g., *Reilinger et al.*, 2000; *Tibi et al.*, 2001; *Bürgmann et al.*, 2002]. We have inverted the coseismic GPS data reported by *Reilinger et al.* [2000], for the best fitting strain field without assuming any particular mechanical behavior (Figure 10). The result, consistent with the mechanical models, is an excellent example of the kinematics of elastic rebound: CCW vertical axis rotation on either side of the fault is accompanied by clockwise rotation across the fault. The asymmetric tails of CW rotation are effects produced by the two tip lines of the fault.

[50] The CCW rotation associated with elastic strain release, however, occurs only during the coseismic deformation and to a lesser extent immediate postseismic slip. If one were able to sample across more than one seismic cycle, the pattern of longer-term permanent deformation would appear similar to the interseismic deformation, especially for stations at or beyond the limit of the "halo" of elastic
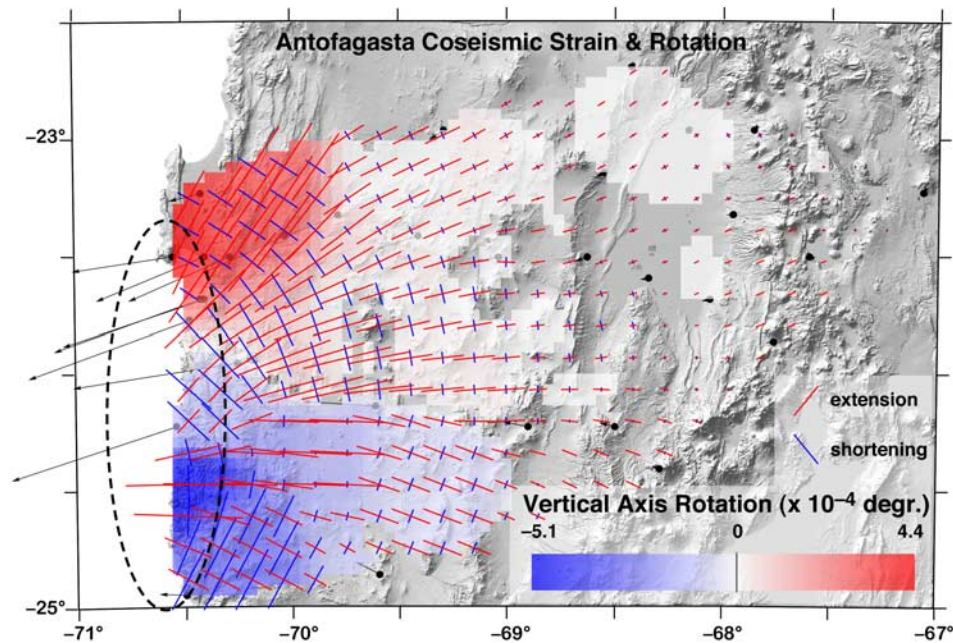
Figure 12. Coseismic vertical axis rotation rate and principal infinitesimal strain rate axes for the 1995 *M*8.1 Antofagasta earthquake. Analyzed data are from *Klotz et al.* [1999]. Dashed black ellipse shows the general extent of the Antofagasta rupture segment [*Pritchard et al.*, 2006].

strain accumulation on the fault. We illustrate this point with the analysis of two synthetic models, one an interseismic, elastically locked strike-slip fault (Figure 11a) and the other a fault that either slips continuously (and permanently) or that has experienced one complete seismic cycle (Figure 11b), both moving at the same average yearly rate. This exercise shows that where both plates are sampled to a density equivalent to that in modern regional campaign GPS networks, permanent and elastic interseismic strains are indistinguishable. Because more than 90% of the elastic interseismic strain occurs within 100 km of the strike-slip fault, future GPS networks will have to have average spacings of 10–20 km or less to capture the elastic interseismic deformation.

[51] Maps of active faulting for the region, and the occurrence of the 1967 earthquake on a subparallel fault south of the 1999 fault break show that the rupture zone of the 1999 event is certainly not the only east-west strike-slip fault in the region [*Şengör et al.*, 2004]. Over geologic time, the elastic strain due to interseismic locking of the North Anatolian plate boundary can be partially relieved by slip on any one of those traces as they are loaded toward failure by the strain accumulated on the plate boundary. The overall combined effect of discrete, and generally sparse, GPS networks with the finite width of interseismic elastic bending is that geologic timescale deformation is entirely consistent in orientation with instantaneous GPS measured deformation (Figure 11).

4.5.2. The 1995 *M*8.1 Antofagasta Earthquake

[52] Like the Izmit event, a relatively dense GPS network was deployed in the region of Antofagasta, Chile just prior

to the *M*8.1 plate boundary event that occurred in July 1995 [*Delouis et al.*, 1998; *Delouis et al.*, 1997; *Klotz et al.*, 2001, 1999; *Pritchard et al.*, 2002; *Ruegg et al.*, 1996]. However, whereas Izmit was a near-vertical strike-slip fault, Antofagasta was a low-angle subduction zone earthquake. Because of this geometry and the fact that much of the subduction thrust lies offshore, only the hanging wall of the fault zone can be sampled geodetically at tens of kilometers distance from the fault itself.

[53] Whereas the coseismic rotation axes calculated for Izmit plunge parallel to the fault dip, those calculated for Antofagasta (Figure 12) are at a high angle to the fault surface and the pattern of rotation is related to terminations of the buried subsurface rupture (schematic dashed oval in Figure 12). CCW rotation occurs over the southern termination and CW over the northern limit. At the center of the rupture zone, coseismic rebound produces east-west to NE-SW principal horizontal extension, perpendicular to local normal faults in the Chilean forearc and parallel to interseismic principal shortening elsewhere along the coast over the locked segments. Cracks striking parallel to upper plate normal faults were observed to open during the 1995 event [*González et al.*, 2003], and elsewhere along the South American forearc extensive suites of trench parallel open cracks are present [*Loveless et al.*, 2005]. Because of the rotation over the terminations of the rupture zone, principal horizontal strain axes are also rotated such that shortening is locally at a high angle to the trace of normal faults in those regions. Though there is no evidence that any of those faults moved during the 1995 event, recent field-
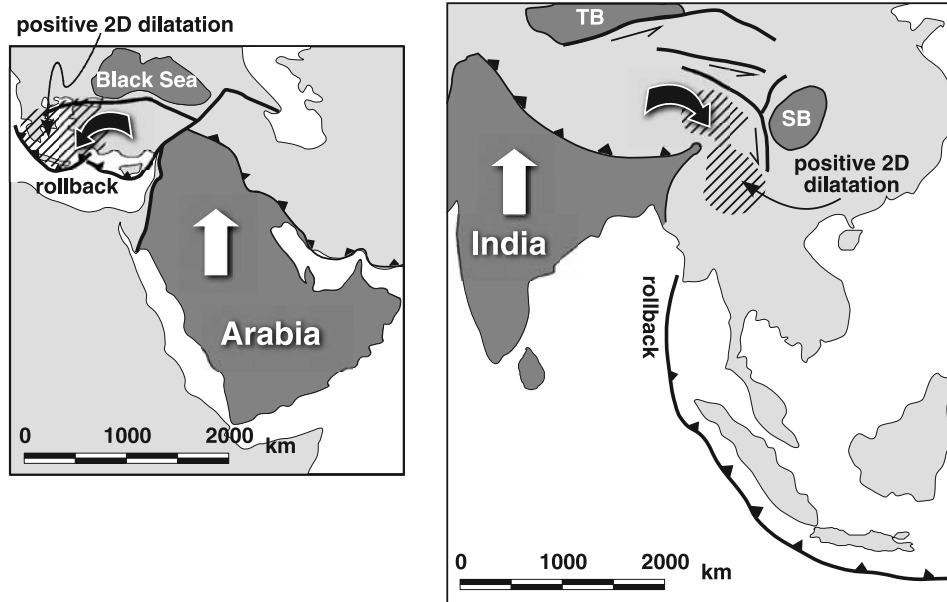
Figure 13. Anatolia and Tibet as the mirror images of one another, highlighting the relationship between possible trench rollback and positive 2-D dilatation. Both maps are constructed at the same scale. Rigid, little deformed continental blocks shown in dark gray. TB, Tarim basin; SB, Sichuan basin. Heavy black arrows show sense of rotation.

work has shown that in the past, several of these faults have been reactivated as reverse faults [*Loveless et al.*, 2006].

[54] Thus, at least some permanent structures of the forearc (surface tension cracks) indicative of E-W extension are coseismic, but the normal faults display a more complicated relationship to the coseismic strain field and may well be due to interseismic flexure. Extensional strain due to elastic rebound for the Antofagasta event diminishes to well below background levels of interseismic shortening east of the volcanic arc.

5. Conclusions

[55] Regional GPS networks are now becoming sufficiently dense that one can, with increasing confidence, calculate the full two-dimensional velocity gradient tensor rather then rely on one-dimensional transects. The 2-D tensor provides additional insight by allowing one to calculate the vertical axis rotation and dilatation rate tensors. Furthermore, the principal horizontal strain rate axes are not always obvious from examination of the velocity vectors alone. Applying this approach to the three plateaus examined here, we conclude:

[56] 1. There are broad coherent domains of regionally consistent strain and rotation rate. Those domains in all three orogens are generally consistent with other short-term (e.g., earthquakes, Quaternary faulting) and long-term (geological and paleomagnetic) indicators of orogenic strain. The orientations of the interseismic strain rate axes and sense of rotation rates should be consistent with geological structures where there are GPS stations on both sides of the faults. The elastic interseismic deformation is nonpermanent

only in that it has yet to be converted to permanent deformation via earthquakes, either on the locked plate or block boundary or on other faults in the region affected by the elastic deformation.

[57] 2. The magnitudes of strain and rotation rate are difficult to interpret because of the irregular nature of current GPS networks, the variation in smoothing algorithms used, and the inherent spatial dependency of strain, itself.

[58] 3. The instantaneous deformation of the noncollisional plateau of the central Andes is entirely different from the two collisional plateaus. The Altiplano is dominated by shortening and thickening with vertical axis rotation produced by distributed simple shear due to orogen parallel gradients in shortening on either side of the topographic symmetry axis. The 2-D dilatation rate in the central Andes is everywhere negative. Because of the low-angle thrust faults bordering both sides of the orogen, the central Andes are likely to be dominated by their elastic, interseismic deformation field.

[59] 4. Shortening plays an important, but secondary role in Tibet and a minor role in much of Anatolia. Instead those plateaus are dominated by the rotation of blocks with relatively minor internal deformation, bounded by narrower zones with opposite sense vertical axis rotation that probably represents the shearing at the edge of the rotating blocks. This rotation is probably a rigid body rotation in contrast to the simple shear rotation in the central Andes.

[60] 5. Anatolia and Tibet are the mirror images of one another (Figure 13), not only in terms of their gross structural geometry, but also, for the regions of positive 2-D dilatation rate on the outboard side of, and probably linked to, the

rotating blocks. The region of positive dilatation rate in the Aegean and western Anatolia is demonstrably a zone of thinning and subsidence and is fundamentally related to rollback of the Hellenic Trench. Positive dilatation rate in eastern Tibet and Yunnan Province, China, might conceivably be related to rollback of the more distant Burma-Sumatra trench but is a region of active uplift. The old rigid cratonal blocks surrounding Tibet, and specifically the Sichuan block to the east of Tibet, may limit the extent to which lithospheric flow can accommodate rollback there.

[61] Current 2-D GPS networks are adequate to resolve first-order regional-scale instantaneous strain variations. However, resolution of some of the issues raised here must await the deployment of dense, continuous GPS networks. Such networks, scaled to the dimensions of the problems one wishes to study, will provide more regular temporal sampling allowing one to calculate more reliably near fault interseismic strain. More importantly, they will bring a critical third dimension of velocity measurement, allowing one to calculate the full 3-D velocity gradient tensor. Furthermore, deployment of dense networks of continuous GPS stations can be used in conjunction with differential radar interferometry to provide a more spatially and temporally complete snapshot of tectonic deformation.

References

Allmendinger, R. W., and T. Gubbels (1996), Pure and simple shear plateau uplift, Altiplano-Puna, Argentina, and Bolivia, *Tectonophysics*, *259*(1–3), 1–14.

Allmendinger, R. W., G. González, J. Yu, G. D. Hoke, and B. L. Isacks (2005a), Trench-parallel shortening in the northern Chilean forearc: Tectonic and climatic implications, *Geol. Soc. Am. Bull.*, *117*(1), 89–104.

Allmendinger, R. W., R. Smalley, M. Bevis, H. Caprio, and B. Brooks (2005b), Bending the Bolivian orocline in real time, *Geology*, *33*, 905–908.

Armijo, R., and R. Thiele (1990), Active faulting in northern Chile: Ramp stacking and lateral decoupling along a subduction plate boundary?, *Earth Planet. Sci. Lett.*, *98*(1), 40–61.

Armijo, R., P. Tapponnier, J. L. Mercier, and T. L. Han (1986), Quaternary extension in southern Tibet: Field observations and tectonic implications, *J. Geophys. Res.*, *91*, 13,803–13,872.

Avouac, J. P., P. Tapponnier, M. Bai, H. You, and G. Wang (1993), Active thrusting and folding along the northern Tien Shan, and late Cenozoic rotation of the Tarim relative to Dzungaria and Kazakhstan, *J. Geophys. Res.*, *98*, 6755–6804.

Banerjee, P., and R. Bürgmann (2002), Convergence across the northwest Himalaya from GPS measurements, *Geophys. Res. Lett.*, *29*(13), 1652, doi:10.1029/2002GL015184.

Beaumont, C., R. A. Jamieson, M. H. Nguyen, and B. Lee (2001), Himalayan tectonics explained by extrusion of a low-viscosity crustal channel coupled to focused surface denudation, *Nature*, *414*, 738–742.

Beaumont, C., R. A. Jamieson, M. H. Nguyen, and S. Medvedev (2004), Crustal channel flows: 1. Numerical models with applications to the tectonics of the Himalayan-Tibetan orogen, *J. Geophys. Res.*, *109*, B06406, doi:10.1029/2003JB002809.

Bevis, M., E. Kendrick, J. R. Smalley, B. A. Brooks, R. W. Allmendinger, and B. L. Isacks (2001), On the strength of interplate coupling and the rate of back arc convergence in the central Andes: An analysis of the interseismic velocity field, *Geochem. Geophys. Geosyst.*, *2*(11), doi:10.1029/2001GC000198.

Bilham, R. (2006), Dangerous tectonics, fragile buildings, and tough decisions, *Science*, *311*, 1873–1875.

Bilham, R., V. K. Gaur, and P. Molnar (2001), Himalayan seismic hazard, *Science*, *293*, 1442–1444.

Brooks, B. A., M. Bevis, R. Smalley Jr., E. Kendrick, R. Manceda, E. Lauría, R. Maturana, and M. Araujo

(2003), Crustal motion in the southern Andes (26°–36°S): Do the Andes behave like a microplate?, *Geochem. Geophys. Geosyst.*, *4*(10), 1085, doi:10.1029/2003GC000505.

Bürgmann, R., M. E. Ayhan, E. J. Fielding, T. J. Wright, S. McClusky, B. Aktug, C. Demir, O. Lenk, and A. Türkezer (2002), Deformation during the 12 November 1999 Düzce, Turkey, earthquake, from GPS and InSAR data, *Bull. Seismol. Soc. Am.*, *91*, 161–171.

Chinn, D. S., and B. L. Isacks (1983), Accurate source depths and focal mechanisms of shallow earthquakes in western South America and in the New Hebrides island arc, *Tectonics*, *2*, 529–564.

Cladouhos, T. T., R. W. Allmendinger, B. Coira, and E. Farrar (1994), Late Cenozoic deformation in the central Andes: Fault kinematics from the northern Puna, northwest Argentina, and southwest Bolivia, *J. South Am. Earth Sci.*, *7*, 209–228.

Clark, M. K., and L. H. Royden (2000), Topographic ooze: Building the eastern margin of Tibet by lower crustal flow, *Geology*, *28*, 703–706.

Clark, M. K., L. M. Schoenbohm, L. H. Royden, K. X. Whipple, B. C. Burchfiel, X. Zhang, W. Tang, E. Wang, and L. Chen (2004), Surface uplift, tectonics, and erosion of eastern Tibet from large-scale drainage patterns, *Tectonics*, *23*, TC1006, doi:10.1029/2002TC001402.

Clark, M. K., M. A. House, L. H. Royden, K. X. Whipple, B. C. Burchfiel, X. Zhang, and W. Tang (2005), Late Cenozoic uplift of southeastern Tibet, *Geology*, *33*, 525–528.

DeCelles, P. G., D. M. Robinson, and G. Zandt (2002), Implications of shortening in the Himalayan fold-thrust belt for uplift of the Tibetan Plateau, *Tectonics*, *21*(6), 1062, doi:10.1029/2001TC001322.

Delouis, B., et al. (1997), The M_w = 8.0 Antofagasta (northern Chile) earthquake of 30 July 1995: A precursor to the end of the large 1877 gap, *Bull. Seismol. Soc. Am.*, *87*, 427–445.

Delouis, B., H. Philip, L. Dorbath, and A. Cisternas (1998), Recent crustal deformation in the Antofagasta region (northern Chile) and the subduction process, *Geophys. J. Int.*, *132*, 302–338.

Dupont-Nivet, G., R. F. Butler, A. Yin, and X. Chen (2002), Paleomagnetism indicates no Neogene rotation of the Qaidam Basin in northern Tibet during Indo-Asian collision, *Geology*, *30*, 263–266.

Echavarría, L., R. Hernández, R. W. Allmendinger, and J. Reynolds (2003), Subandean thrust and fold belt

of northwestern Argentina: Geometry and timing of the Andean evolution, *AAPG Bull.*, *87*(6), 965–985.

England, P., and P. Molnar (2005), Late Quaternary to decadal velocity fields in Asia, *J. Geophys. Res.*, *110*, B12401, doi:10.1029/2004JB003541.

Flesch, L. M., W. E. Holt, P. G. Silver, M. Stephenson, C.-Y. Wang, and W. W. Chan (2005), Constraining the extent of crust-mantle coupling in central Asia using GPS, geologic, and shear wave splitting data, *Earth Planet. Sci. Lett.*, *238*, 248–268.

Friedrich, A., B. Wernicke, N. Niemi, R. Bennett, and J. Davis (2003), Comparison of geodetic and geologic data from the Wasatch region, Utah, and implications for the spectral character of Earth deformation at periods of ten to ten million years, *J. Geophys. Res.*, *108*(B4), 2199, doi:10.1029/2001JB000682.

Gephart, J. W. (1994), Topography and subduction geometry in the central Andes: Clues to the mechanics of a noncollisional orogen, *J. Geophys. Res.*, *99*, 12,279–12,288.

Gonzalez, G., J. Cembrano, D. Carrizo, A. Macci, and H. Schneider (2003), The link between forearc tectonics and Pliocene–Quaternary deformation of the Coastal Cordillera, northern Chile, *J. South Am. Earth Sci.*, *16*, 321–342.

Gubbels, T., B. Isacks, and E. Farrar (1993), High-level surfaces, plateau uplift, and foreland development, Bolivian central Andes, *Geology*, *21*, 695–698.

Gürsoy, H., J. D. A. Piper, and O. Tatara (2003), Neotectonic deformation in the western sector of tectonic escape in Anatolia: Palaeomagnetic study of the Afyon region, central Turkey, *Tectonophysics*, *374*, 57–79.

Halim, N., Y. Chen, and J. P. Cogné (2003), A first palaeomagnetic study of Jurassic formations from the Qaidam basin, northeastern Tibet, China—Tectonic implications, *Geophys. J. Int.*, *153*, 20–26.

Isacks, B. L. (1988), Uplift of the central Andean plateau and bending of the Bolivian orocline, *J. Geophys. Res.*, *93*, 3211–3231.

Jackson, J., and D. McKenzie (1984), Active tectonics of the Alpine–Himalayan belt between western Turkey and Pakistan, *Geophys. J. R. Astron. Soc.*, *77*, 185–246.

Kahle, H.-G., M. Cocard, Y. Peter, A. Geiger, R. Reilinger, A. Barka, and G. Veis (2000), GPS-derived strain rate field within the boundary zones of the Eurasian, African, and Arabian plates, *J. Geophys. Res.*, *105*, 23,353–23,370.

Kendrick, E., M. Bevis, R. Smalley, and B. Brooks (2001), An integrated crustal velocity field for the central Andes, *Geochem. Geophys. Geosyst.*, *2*(11), doi:10.1029/2001GC000191.

Khazaradze, G., and J. Klotz (2003), Short- and long-term effects of GPS measured crustal deformation rates along the south central Andes, *J. Geophys. Res.*, *108*(B6), 2289, doi:10.1029/2002JB001879.

Klotz, J., et al. (1999), GPS-derived deformation of the central Andes including the 1995 Antofagasta *Mw* = 8.0 earthquake, *Pure Appl. Geophys.*, *154*, 709 – 730.

Klotz, J., G. Khazaradze, D. Angermann, C. Reigber, R. Perdomo, and O. Cifuentes (2001), Earthquake cycle dominates contemporary crustal deformation in central and southern Andes, *Earth Planet. Sci. Lett.*, *193*, 437 – 446.

Koons, P. O., A. Barker, T. L. Pavlis, Y. Liu, S. Sol, P. K. Zeitler, and A. Meltzer (2006), Vorticity, erosion, and crust: Mantle coupling at plate corners in south east Alaska and south east Tibet, *Eos Trans. AGU*, *87*(52), Fall Meet. Suppl., Abstract T32B-07.

Kumar, S., S. G. Wesnousky, T. K. Rockwell, R. W. Briggs, V. C. Thakur, and R. Jayangondaperumal (2006), Paleoseismic evidence of great surface rupture earthquakes along the Indian Himalaya, *J. Geophys. Res.*, *111*, B03304, doi:10.1029/2004JB003309.

Lamb, S. (2001a), Vertical axis rotation in the Bolivian orocline, South America: 1. Paleomagnetic analysis of Cretaceous and Cenozoic rocks, *J. Geophys. Res.*, *106*, 26,605 – 26,632.

Lamb, S. (2001b), Vertical axis rotation in the Bolivian orocline, South America: 2. Kinematic and dynamical implications, *J. Geophys. Res.*, *106*, 26,633 – 26,653.

Le Pichon, X., and J. Angelier (1979), The Hellenic arc and trench system: A key to the neotectonic evolution of the eastern Mediterranean area, *Tectonophysics*, *60*(1 – 2), 1 – 42.

Liu, Y., W. Tang, Q. Zhang, J. Zhao, Z. Chen, and P. O. Koons (2006), GPS monitoring of crustal deformation around the eastern Himalayan syntaxis, *Eos Trans. AGU*, *87*(52), Fall Meet. Suppl., Abstract T23B-0478.

Loveless, J. P., G. D. Hoke, R. W. Allmendinger, G. González, B. L. Isacks, and D. A. Carrizo (2005), Pervasive cracking of the northern Chilean Coastal Cordillera: New evidence of forearc extension, *Geology*, *33*, 973 – 976.

Loveless, J., M. Pritchard, and R. W. Allmendinger (2006), Motion of upper plate faults during subduction zone earthquakes: The curious case of the Atacama fault in northern Chile, *Seismol. Res. Lett.*, *77*, 291.

Malvern, L. E. (1969), *Introduction to the Mechanics of a Continuous Medium*, Prentice-Hall, Englewood Cliffs, N. J.

Marrett, R. A., R. W. Allmendinger, R. N. Alonso, and R. E. Drake (1994), Late Cenozoic tectonic evolution of the Puna Plateau and adjacent foreland, northwestern Argentine Andes, *J. South Am. Earth Sci.*, *7*, 179 – 208.

McClusky, S., et al. (2000), Global Positioning System constraints on plate kinematics and dynamics in the eastern Mediterranean and Caucasus, *J. Geophys. Res.*, *105*, 5695 – 5719.

Meade, B. J. (2007), Present-day kinematics at the India – Asia collision zone, *Geology*, *35*, 81 – 84, doi:10.1130/G22924A.1.

Meade, B. J., and B. H. Hager (2005), Block models of crustal motion in southern California constrained by GPS measurements, *J. Geophys. Res.*, *110*, B03403, doi:10.1029/2004JB003209.

Menke, W. (1984), *Geophysical Data Analysis: Discrete Inverse Theory*, 260 pp., Academic, Orlando, Fla.

Molnar, P., and W. P. Chen (1983), Focal depths and fault plane solutions of earthquakes under the Tibetan Plateau, *J. Geophys. Res.*, *88*, 1180 – 1196.

Molnar, P., and H. Lyon-Caen (1989), Fault plane solutions of earthquakes and active tectonics of the Tibetan Plateau and its margins, *Geophys. J. Int.*, *99*, 123 – 153.

Nelson, K. D., et al. (1996), Partially molten middle crust beneath southern Tibet, synthesis of project INDEPTH results, *Science*, *274*, 1684 – 1688.

Niemeyer, H., G. González, and E. Martinez-De Los Rios (1996), Evolución tectónica cenozoica del margen continental activo de Antofagasta, norte de Chile, *Rev. Geol. Chile*, *23*(2), 165 – 186.

Norabuena, E., L. Leffler-Griffin, A. Mao, T. Dixon, S. Stein, I. S. Sacks, L. Ocola, and M. Ellis (1998), Space geodetic observations of Nazca – South America convergence across the central Andes, *Science*, *279*, 358 – 362.

Okada, Y. (1985), Surface deformation due to shear and tensile faults in a half-space, *Bull. Seismol. Soc. Am.*, *75*, 1135 – 1154.

Pancha, A., J. G. Anderson, and C. Kreemer (2006), Comparison of seismic and geodetic scalar moment rates across the basin and range province, *Bull. Seismol. Soc. Am.*, *96*, 11 – 32.

Press, W. H., B. P. Flannery, S. A. Teukolsky, and W. T. Vetterling (1986), *Numerical Recipes: The Art of Scientific Computing*, 818 pp., Cambridge Univ. Press, Cambridge, U. K.

Pritchard, M. E., M. Simons, P. A. Rosen, S. Hensley, and F. H. Webb (2002), Coseismic slip from the 1995 July 30 *Mw* = 8.1 Antofagasta, Chile, earthquake as constrained by InSAR and GPS observations, *Geophys. J. Int.*, *150*, 362 – 376.

Pritchard, M., C. Ji, and M. Simons (2006), Distribution of slip from 11 $M_w > 6$ earthquakes in the northern Chile subduction zone, *J. Geophys. Res.*, *111*, B10302, doi:10.1029/2005JB004013.

Reilinger, R. E., et al. (2000), Coseismic and postseismic fault slip for the 17 August 1999, *M* = 7.5, Izmit, Turkey earthquake, *Science*, *289*, 1519 – 1524.

Reilinger, R., et al. (2006), GPS constraints on continental deformation in the Africa – Arabia – Eurasia continental collision zone and implications for the dynamics of plate interactions, *J. Geophys. Res.*, *111*, B05411, doi:10.1029/2005JB004051.

Royden, L. (1993), The tectonic expression of slab pull at continental convergent boundaries, *Tectonics*, *12*, 303 – 325.

Ruegg, J. C., et al. (1996), The M_w = 8.1 Antofagasta (north Chile) earthquake of July 30, 1995: First results from teleseismic and geodetic data, *Geophys. Res. Lett.*, *23*, 917 – 920.

Savage, J. C. (1983), A dislocation model of strain accumulation and release at a subduction zone, *J. Geophys. Res.*, *88*, 4984 – 4996.

Savage, J. C., and R. O. Burford (1973), Geodetic determination of relative plate motion in central California, *J. Geophys. Res.*, *78*, 832 – 845.

Schoenbohm, L. M., B. C. Burchfiel, C. Liangzhong, and Y. Jiyun (2006), Miocene to present activity along the Red River fault, China, in the context of continental extrusion, upper-crustal rotation, and lower-crustal flow, *Geol. Soc. Am. Bull.*, *118*(5/6), 672 – 688.

Sébrier, M., J. L. Mercier, F. Mégard, and G. Laubacher (1985), Quaternary normal and reverse faulting and the state of stress in the central Andes of south Peru, *Tectonics*, *4*, 739 – 780.

Şengör, A. M. C., N. Görür, F. Şaroğlu (1985), Strike-slip faulting and related basin formation in zones of tectonic escape: Turkey as a case study, in *Strike-Slip Faulting and Basin Formation*, edited by K. T. Biddle and N. Christie-Blick, *Spec. Publ. Soc. Econ. Paleontol. Mineral.*, *37*, 227 – 264.

Şengör, A. M. C., O. Tuysuz, C. Imren, M. Sakinc, H. Eyidogan, N. Görür, X. Le Pichon, and C. Rangin (2004), The north Anatolian fault: A new look, *Annu. Rev. Earth Planet. Sci.*, *33*, 1 – 75.

Shen, Z. K., D. D. Jackson, and B. X. Ge (1996), Crustal deformation across and beyond the Los Angeles basin from geodetic measurements, *J. Geophys. Res.*, *101*, 27,957 – 27,980.

Tatar, O., J. D. A. Piper, R. G. Park, and H. Gursoy (1995), Paleomagnetic study of block rotations in the Niksar overlap region of the north Anatolian fault zone, central Turkey, *Tectonophysics*, *244*, 251 – 266.

Tibi, R., G. Bock, Y. Xia, M. Baumbach, H. Grosser, C. Milkereit, S. Karakisa, S. Zunbul, R. Kind, and J. Zschau (2001), Rupture processes of the 1999 August 17 Izmit and November 12 Duzce (Turkey) earthquakes, *Geophys. J. Int.*, *144*, F1 – F7.

Turcotte, D. L., and G. Schubert (1982), *Geodynamics: Applications of Continuum Physics to Geological Problems*, 450 pp., John Wiley, New York.

Van der Woerd, J., P. Tapponnier, F. J. Ryerson, A. S. Meriaux, B. Meyer, Y. Gaudemer, R. C. Finkel, M. W. Caffee, Z. Guoguang, and X. Zhiqin (2002), Uniform postglacial slip-rate along the central 600 km of the Kunlun fault (Tibet), from [26]Al, [10]Be, and ^{14}C dating of riser offsets, and climatic origin of the regional morphology, *Geophys. J. Int.*, *148*, 356 – 388.

Williams, G. D., and S. J. Kane (1999), Three-dimensional restoration algorithm and finite strain in thrust systems, paper presented at Thrust Tectonics Conference, Univ. of London, London.

Zhang, P., et al. (2004), Continuous deformation of the Tibetan Plateau from Global Positioning System data, *Geology*, *32*, 809 – 812.

R. W. Allmendinger and J. Loveless, Department of Earth and Atmospheric Sciences, Cornell University, Ithaca, NY 14853-1504, USA. (rwa1@cornell.edu)

R. Reilinger, Department of Earth, Atmospheric, and Planetary Sciences, Massachusetts Institute of Technology, 42 Carleton Street, Cambridge, MA 02139, USA.